ChemistrySelect

ChemistrySelect

Chemistry Europe
European Chemical
Societies Publishing

RESEARCH ARTICLE OPEN ACCESS

Exploring the Photogenerated Charge Transfer Mechanism in $Cu_2O@MoS_2$ Heterojunction Photocatalyst Using Transient Absorption Spectroscopy

Meng Zhang[1] | J. Dembicky[1] | Zuolong Chen[1] | Xiyang Wang[1] | Sha Li[2] | Benjamin T. Diroll[3] | William Wong[4] | Ian McNulty[5] | Jamie H. Warner[2,6] | Richard D. Schalller[3,7] | Tijana Rajh[3,8] | Yimin A. Wu[1]

[1]Department of Mechanical and Mechatronics Engineering, Waterloo Institute of Nanotechnology, Waterloo, Canada | [2]Department of Materials, University of Oxford, Oxford, UK | [3]Center For Nanoscale Materials, Argonne National Laboratory, Lemont, Illinois, USA | [4]Department of Electrical and Computer Engineering, University of Waterloo, Waterloo, Canada | [5]Max IV Laboratory, Lund University, Lund, Sweden | [6]Walker Department of Mechanical Engineering, The University of Texas at Austin, Austin, Texas, USA | [7]Department of Chemistry, Northwestern University, Evanston, Illinois, USA | [8]School of Molecular Sciences, Arizona State University, Tempe, Arizona, USA

Correspondence: Zuolong Chen (zuolong.chen@uwaterloo.ca) | Yimin A. Wu (yimin.wu@uwaterloo.ca)

Received: 1 January 2026 | **Revised:** 20 April 2026 | **Accepted:** 14 May 2026

Keywords: carrier dynamics | co_2 reduction | heterojunction | photocatalysis | transient absorption spectroscopy

ABSTRACT

Both heterojunction and core–shell photocatalysts have demonstrated promising performance in photocatalytic CO_2 conversions to fuels. However, fundamental knowledge of heterojunctions in core–shell structures is highly desired to facilitate the design of future photocatalysts. By combining advanced experimental characterizations and density functional theory (DFT) calculations, the role of the $Cu_2O@MoS_2$ heterojunction in photocatalytic CO_2 conversions to fuels was investigated. We discovered that the charge dynamics and electron transfer properties of $Cu_2O@MoS_2$ photocatalysts are altered by the heterojunction and Cu_2O underlayer due to the electron transfer from Cu_2O to MoS_2 and the change in CO_2 adsorption strength on the hybrid catalyst surface. Consequently, more electrons can travel to the surrounding liquid environment to be consumed by CO_2 reduction. This study provides experimental and theoretical investigations of the fundamental mechanisms of heterojunction core–shell photocatalysts.

1 | Introduction

Some of the greatest challenges facing our planet in this century include developing sustainable energy sources to prepare for the depletion of fossil fuels and curbing climate change driven by anthropogenic CO_2 emissions [1, 2]. Among various renewable options, solar energy stands out as the most abundant and universally accessible resource, offering a viable long-term foundation for a sustainable global energy system. Converting solar energy directly into chemical fuels is particularly attractive, as it enables energy storage, grid decarbonization, and the production of carbon-neutral feedstocks [2, 3, 4, 5–7]. Photocatalytic CO_2 reduction has been demonstrated to be a one-step, efficient, and scalable way for directly converting solar energy into chemical fuels with the help of photocatalysts such as Cu_2O and MoS_2 [8–12]. However, the efficiency of this process remains limited by rapid charge recombination, insufficient CO_2 adsorption, and competing side reactions. In photocatalytic reactions, the absorption of photons, the separation of electron–hole pairs, the surface redox reactions, and adsorption and desorption of

---

Meng Zhang, J Dembicky, and Zuolong Chen contributed equally to this work.

reactants are the key elemental reaction steps, and semiconductor heterojunctions can be employed to influence such reaction steps [13–15]. Therefore, constructing semiconductor heterojunctions has become a promising approach for improving photocatalytic performance, as they could potentially influence and tune charge recombination rates, adsorption properties at active sites, and electron affinity [16–18].

Here, MoS_2 coated on Cu_2O ($Cu_2O@MoS_2$) is chosen as a model system for this heterojunction strategy for photocatalysis. The free energy of absorbed hydrogen on MoS_2 is close to zero, which makes MoS_2 a suitable catalyst for water splitting [19–22] and CO_2 reduction [10, 23, 24]. Also, MoS_2 sheets can act as a protective coating on the Cu_2O that may prevent photocorrosion [25, 26]. Here, we investigate the role of the heterojunction and the Cu_2O core layer on the MoS_2 photocatalyst for photocatalytic CO_2 reduction. First, we found that MoS_2 coating yields CO instead of CH_3OH as the product of CO_2 reduction. Then, transient absorption spectroscopy characterizations suggest that the charge carrier dynamics and electron transfer rates were affected by the Cu_2O underlayer in the core-shell photocatalyst. Theoretical studies revealed that the Cu_2O core not only transfers electrons to the conduction band of MoS_2 but also enhances CO_2 physisorption, thus increasing the charge transfer rate for CO_2 reduction. Consequently, more electrons can travel to the solution and react with CO_2 molecules near the heterojunction core–shell catalyst. This study provides fundamental knowledge on the reaction mechanism of heterojunction photocatalysts and offer design strategies for advanced photocatalysts for CO_2 reduction.

2 | Results and Discussion

Figure 1 shows the structural characterization of Cu_2O core, MoS_2-coated Cu_2O particles, and MoS_2 flakes. Bare Cu_2O microcrystals were synthesized using a colloidal synthesis route described in Methods, which produces a mixture of cubic and octahedral crystals, as shown in Figure 1a. Chemical vapor deposition (CVD) was used to deposit MoS_2 onto Cu_2O particles, yielding flower-shaped core–shell particles, as shown in Figure 1b. The high-resolution transmission electron microscopy (HRTEM) image in Figure 1c shows MoS_2 coated on Cu_2O ($Cu_2O@MoS_2$) crystals. The flowerlike MoS_2 nanosheets form a high surface area, edge-rich "petals" wrapping/anchoring on the Cu_2O grains and creating an intimate, 3D, porous interface. Therefore, short diffusion paths from Cu_2O into MoS_2 and from MoS_2 to the solution may be provided, favorable to the photocatalytic reaction. MoS_2 flakes with a few layers were synthesized using a liquid exfoliation method [27] with a size of approximately 200 nm, as shown in Figure 1d. MoS_2 flakes showed single-crystal electron diffraction with (100) d spacing of 0.27 nm and (110) d spacing of 0.16 nm in Figure 1e. HRTEM image of MoS_2 showed the lattice fringes of the crystal in Figure 1f. The elemental distributions are presented in Figure 1g, including Cu, O, Mo, and S elements, which confirms that the crystals are $Cu_2O@MoS_2$ heterostructures. Furthermore, x-ray diffraction (XRD) confirmed the successful introduction of MoS_2 (Figure 1h). No Cu_2O phase was detected by XRD, likely due to its low loading or the disruption of its crystal structure during the high-temperature CVD process. However, the more sensitive x-ray photoelectron spectroscopy (XPS) provides clear evidence for the presence of both components. The Cu 2p spectrum (Figure 2a) shows characteristic peaks corresponding predominantly to Cu^+ species, confirming the existence of Cu_2O, with minor contributions from Cu^{2+} attributed to surface oxidation or interfacial effects. The Mo 3d (Figure 2b) exhibits binding energies consistent with Mo^{4+} in MoS_2. In addition, the XPS spectra of Cu and Mo in samples after the photocatalytic reactions are shown in Figure 2c,d, respectively. The shift in Cu oxidation state toward a higher binding energy by ~0.3 eV, along with the existence of Cu^{2+}, confirms that the Cu has been active and oxidized during the reaction, as well as the electron transfer from Cu to Mo under illumination. The energy in Mo toward a lower binding energy by ~0.24 eV confirms that Cu is the active site for the reaction, and the electron transfer from Cu to Mo.

Subsequently, $Cu_2O@MoS_2$ particles were applied in the photocatalytic CO_2 reduction reaction. The reactant CO_2 and products were analyzed by gas chromatography-mass spectrometry (GC-MS). Detailed measurement method can be found in the Experimental section. As demonstrated in Figure 3a,b, CO and methane were produced from photocatalytic CO_2 reduction as products, and the yield of CO is about 5 μmol in a 20 mL reactor after 20 min irradiation time, similar to the data reported in the previous paper [28]. For confirmation, a $^{13}CO_2$ isotope tracer experiment was performed (see Methods). Figure 3c confirmed the formation of ^{13}CO from $^{13}CO_2$ with GCMS analysis. The distinct mass to charge ratios of 16, 29, and 45 correspond to $[O]^+$, $[^{13}CO\bullet]^+$, and $[CO_2\bullet]^+$. The remaining peak at 45 corresponds to unreacted $^{13}CO_2$ in the sealed vial. This finding provides strong evidence that the carbon in CO was derived from CO_2. Due to the thin-film nature of the catalyst and the low product yield, only gaseous products were reliably quantified, while liquid products and apparent quantum efficiency (AQE) could not be accurately determined. Therefore, this work focuses on mechanistic understanding rather than comprehensive performance evaluation. It is interesting to note that MoS_2 alone as an electrocatalyst can reduce CO_2 to CO [23], while Cu_2O as a photocatalyst can reduce CO_2 to methanol [29], highlighting the complementary roles of the two components in the heterostructure.

In order to understand the energetics of heterojunction photocatalysts, UV–vis absorption spectra were measured. The Cu_2O bare crystal showed a distinct absorption peak around 500 nm in Figure 4a. The liquid exfoliated MoS_2 showed characteristic peaks at 670, 610, 448, and 405 nm in Figure 4b, which are consistent with previous reports on multilayer MoS_2 [30]. $Cu_2O@MoS_2$ crystals showed both the characteristic peaks of MoS_2 at 670 and 610 nm and Cu_2O peaks at 500 nm (Figure 4c). The band structure of $Cu_2O@MoS_2$ heterostructures shows a staggered type II band alignment in Figure 4d [31–33]. The CO_2 reduction level is known to be −3.67 eV, which is about 1.23 eV above the valence band of Cu_2O shown in Figure 4d [34]. The band gaps of Cu_2O and MoS_2 are 2.1 and 1. 6 eV, respectively, consistent with the onset value from the UV–vis absorption spectra in Figure 4a–c.

To investigate the light-matter interaction during the photocatalytic process, transient absorption (TA) measurements were performed. Dynamics of the Cu_2O core, MoS_2 flakes, and $MoS_2@Cu_2O$ heterostructure were probed using low-fluence 400 nm excitation to avoid multiexcitonic processes. CO_2 gas was continuously flowed into the ethanol solutions of the

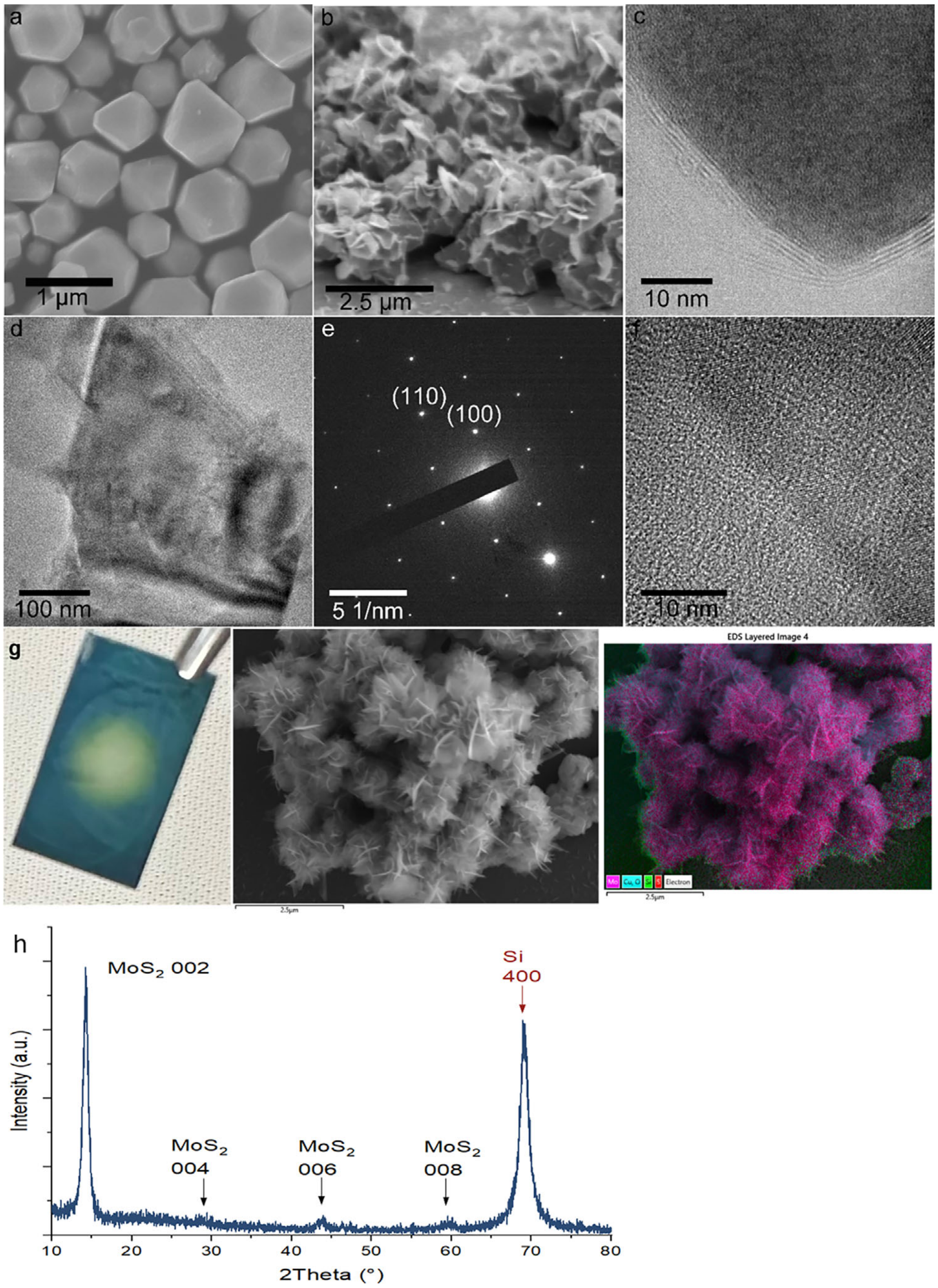

FIGURE 1 | Structural and morphology characterizations. (a) SEM image of Cu_2O bare crystals from colloidal synthesis. (b) SEM image of chemical vapor deposition MoS_2-coated Cu_2O ($Cu_2O@MoS_2$) crystals. (c) HRTEM images on the edges of $Cu_2O@MoS_2$ crystals. (d) MoS_2 flakes from liquid exfoliation. (e) Electron diffraction of MoS_2 flakes. (f) HRTEM images of MoS_2 flakes. (g) Photograph of the CVD-deposited $Cu_2O@MoS_2$ sample on a Si wafer, SEM image of $Cu_2O@MoS_2$ sample, and EDX mapping showing the elemental maps of Cu, O, Mo, S. (h) The XRD pattern of the $Cu_2O@MoS_2$ sample.

samples to saturate the CO_2 concentrations in the solutions. Based on the band alignment in Figure 4d, the TA signal at 511 nm for Cu_2O (Figure 5a,c) is assigned to conduction band electron dynamics, arising from state-filling near the band edge [35]. The 2D plot is used to examine the wavelength-dependent carrier behavior and select the wavelength region of interest. The photoabsorption decay relates to a significantly decreasing population of electrons in the Cu_2O conduction band through recombination or consumption. Both traces start with a sharp spike at t≈0, corresponding to pump scatter and the instrument response. The transient absorption (ΔOD) is positive immediately after time zero and decays toward ~0 over ~6–7 ns. In the presence of CO_2 (black trace), the signal is slightly larger and decays more slowly compared to the CO_2-free condition (red trace). This slower decay indicates that CO_2 molecules suppress electron-hole recombination in Cu_2O. Instead of recombining with valence-band holes, conduction-band electrons are transferred to adsorbed CO_2 species, consistent with CO_2 acting as an electron-trapping/reactive intermediate on the Cu_2O surface.

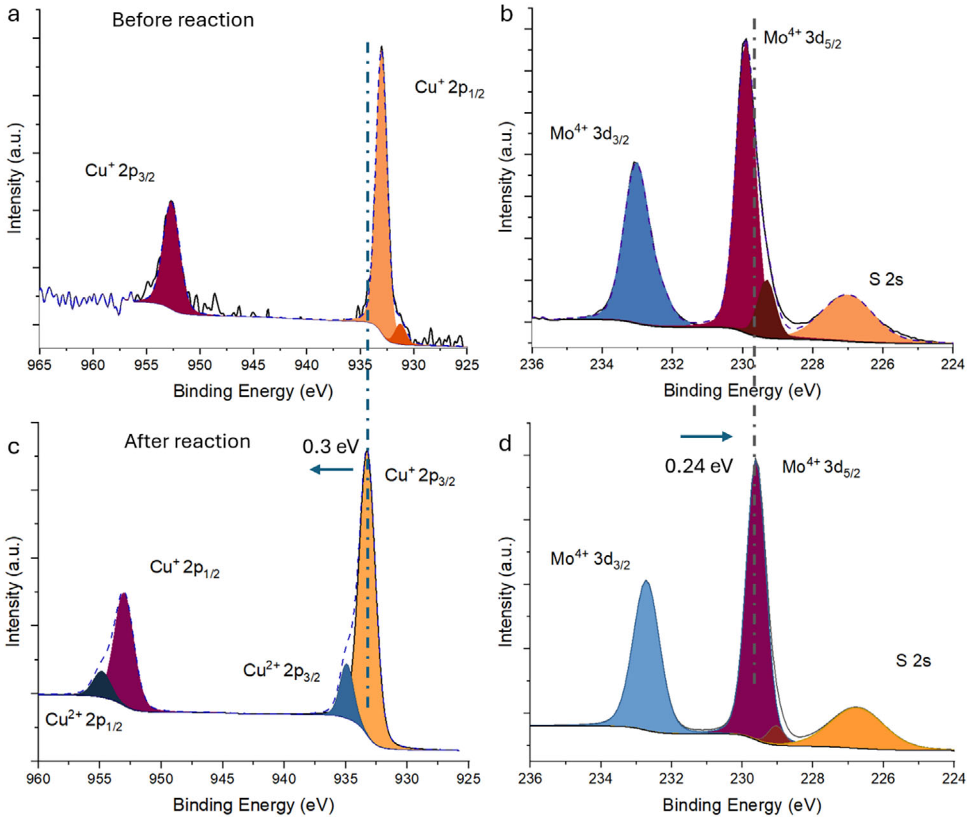

FIGURE 2 | XPS of Cu 2p and Mo 3d before and after photocatalytic reactions.

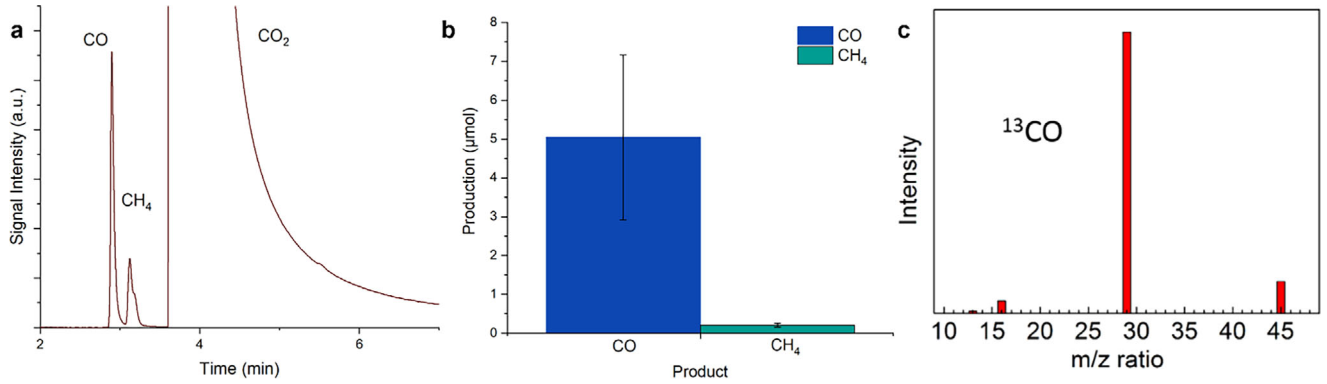

FIGURE 3 | Photocatalytic CO_2 reduction performance of Cu_2O@MoS_2 heterostructures. (a,b) CO and methane production by Cu_2O@MoS_2 heterostructures measured by gas chromatography (GC) during the photocatalytic reaction. (c) Carbon isotope tracer measurement, mass spectra of ^{13}CO production from $^{13}CO_2$ over Cu_2O@MoS_2 obtained by GC-MS analysis after 20 min irradiation time.

MoS_2 exhibits a similar overall TA profile, characterized by a prompt rise, a rapid initial decay, and a long nanosecond tail. The TA signal at 545 nm (Figure 5b,d) is attributed to excitonic transitions near its band edge. However, unlike Cu_2O, the decay dynamics of conduction-band electrons in the MoS_2 flakes show no discernible difference between the CO_2-saturated and CO_2-free conditions (Figure 5b). This observation indicates that CO_2 molecules do not strongly adsorb onto the MoS_2 surface under the experimental conditions. Instead, they remain largely unbound and dispersed in the solution, leaving the electron decay kinetics in MoS_2 unaffected. This is consistent with its band position (Figure 4d), where electron transfer to CO_2 is less favorable without interfacial modification. In this case, the electrons may need to diffuse a long distance to reduce CO_2 molecules. This contrast indicates different reaction mechanisms of CO_2 reduction on Cu_2O and MoS_2, although they were both reported as candidates for CO_2 reduction [23, 24]. The adsorption effect is the dominant effect in Cu_2O since CO_2 adsorbs strongly to the surfaces of Cu_2O [29]. However, the charge separation is the dominant effect in MoS_2 since CO_2 molecules adsorb/desorb

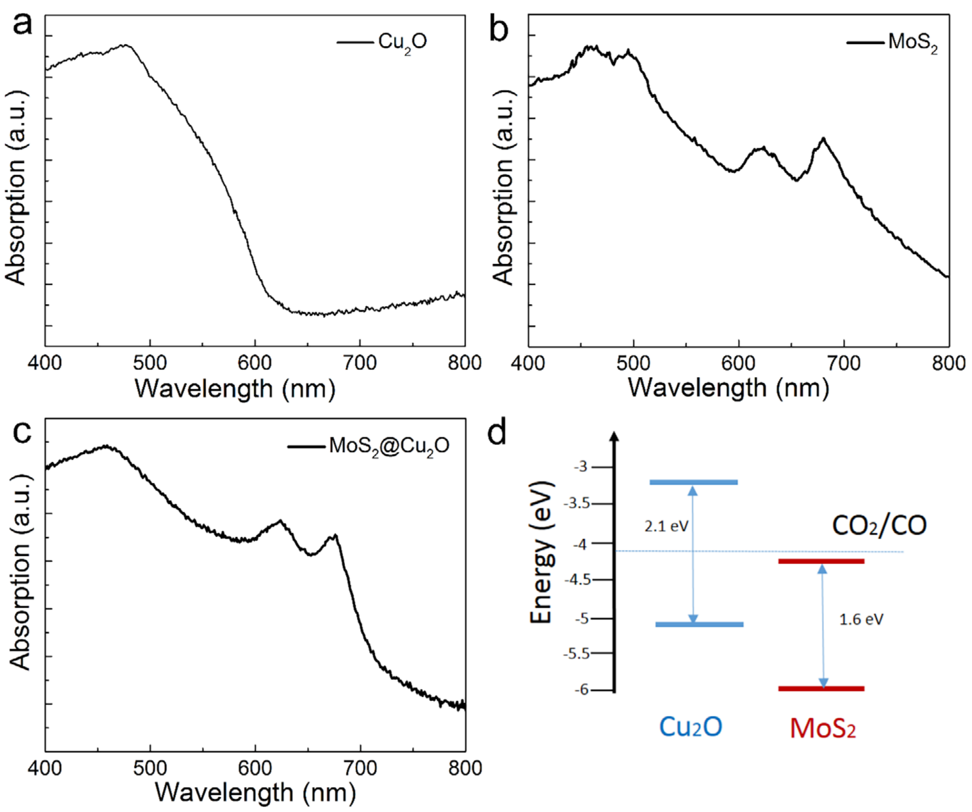

FIGURE 4 | UV–vis absorption and band structure of Cu_2O, MoS_2, and $Cu_2O@MoS_2$ crystals. (a) Cu_2O, (b) MoS_2, (c) MoS_2-coated Cu_2O, and (d) the band structure of $Cu_2O@MoS_2$ heterostructures with CO_2/CO reduction level.

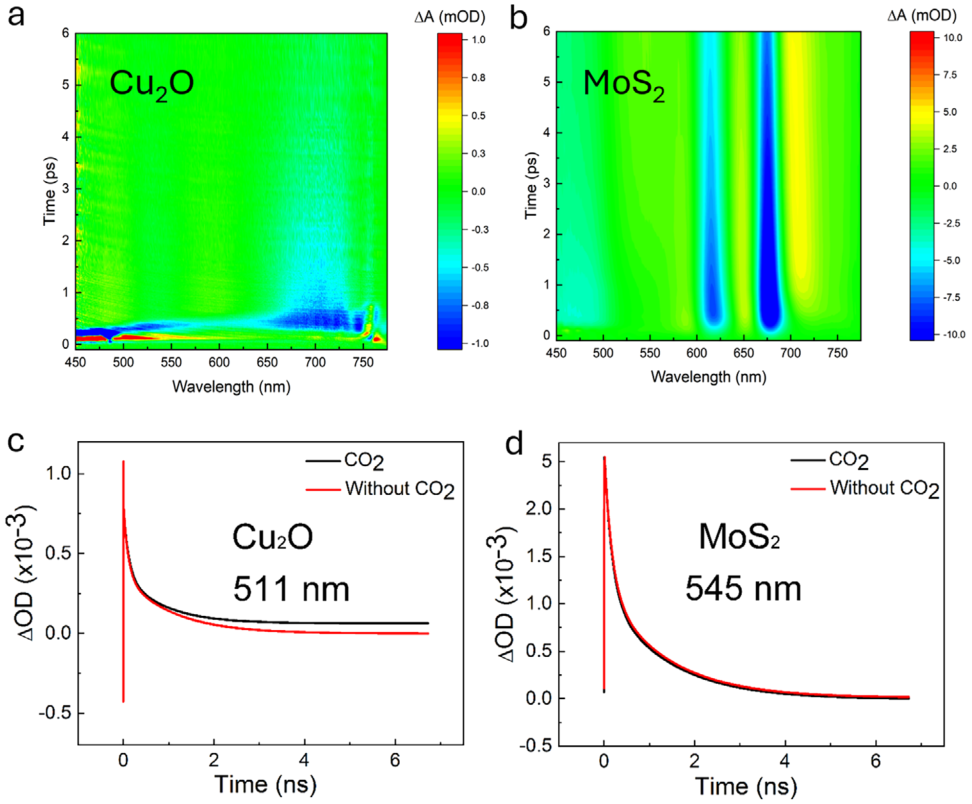

FIGURE 5 | Carrier dynamics by operando transient absorption (TA) spectrum in (a) and (c) bare Cu_2O crystals, and (b) and (d) MoS_2 crystals. The 2D pseudo colored TA in (a) and (b) shows the wavelength-dependent behaviors without CO_2.

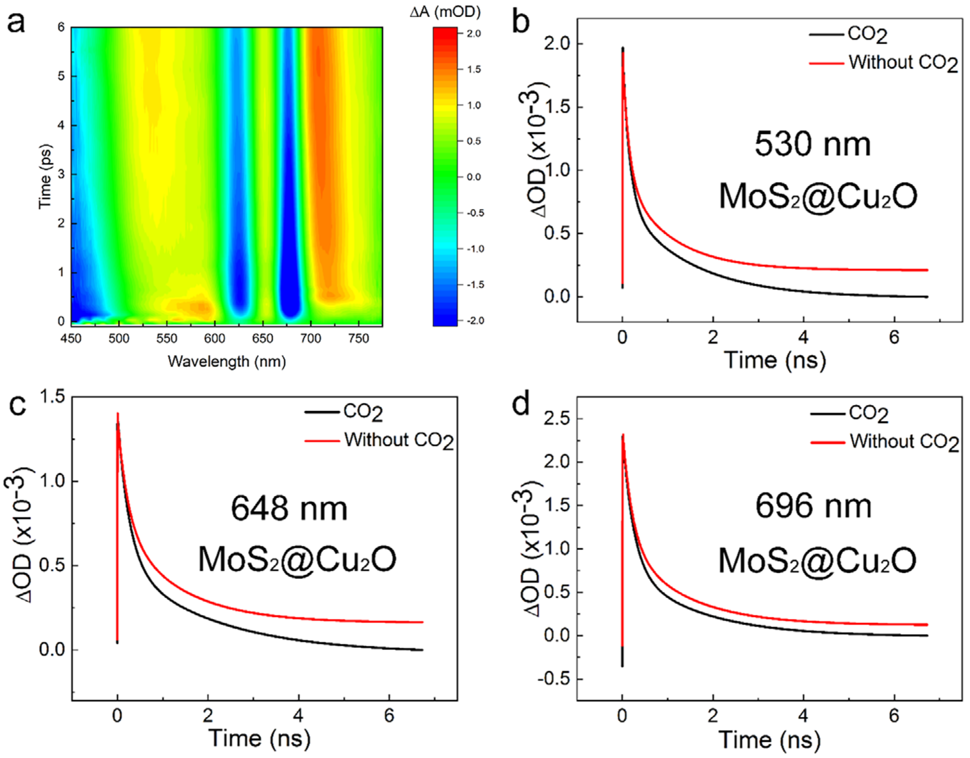

FIGURE 6 | Carrier dynamics of $Cu_2O@MoS_2$ crystals. (a) Operando transient spectrum maps of $Cu_2O@MoS_2$ crystals with CO_2 flow. (b) Carrier dynamics of $Cu_2O@MoS_2$ crystals at 530 nm. (c) Carrier dynamics of $Cu_2O@MoS_2$ crystals at 648 nm. (d) Carrier dynamics of $Cu_2O@MoS_2$ crystals at 696 nm.

quickly from the surfaces. This finding is consistent with CO_2 adsorption isotherms measurement on Cu_2O and MoS_2 [36, 37]. It has about 1 cm^3/g adsorbed CO_2 on Cu_2O surfaces at 1 atmosphere, while it has little or no adsorption of CO_2 on MoS_2 [36, 37].

TABLE 1 | Electron transfer rates k_{ET} (ps^{-1}) during CO_2 reduction processes.

Wavelength (nm)	Cu_2O	MoS_2	MoS_2-coated Cu_2O
511	1.4×10^{-3}	—	—
530	—	—	0.5×10^{-3}
545	—	0.7×10^{-3}	—
648	—	—	0.3×10^{-3}
696	2.6×10^{-3}	0.2×10^{-3}	0.4×10^{-3}

Considering the different mechanisms of CO_2 reduction on Cu_2O core and MoS_2 flakes, transient absorption spectroscopy was employed to probe the carrier dynamics in $Cu_2O@MoS_2$ core-shell heterostructure during CO_2 reduction. Figure 6a shows an operando two-dimensional map of the carrier dynamics using low fluence 400 nm excitation upon the continuous flow of CO_2 gas. Immediately after excitation, broadband signals of mixed sign appear, including regions of positive ΔOD (photo-induced absorption) and negative ΔOD (photo-bleach at resonances). The strongest spectral activity appears around ~520–560 and ~640–700 nm, consistent with Cu_2O-related transitions and MoS_2 A/B exciton region. The band structure of the heterostructure revealed a staggered type II band alignment between Cu_2O and MoS_2 in Figure 4d. The line cuts taken from Figure 6a reveal characteristic photoabsorption peaks at 530, 648, and 696 nm. The corresponding carrier dynamics at these wavelengths are shown in Figures 6b-d. Across all three probe wavelengths, the CO_2-saturated traces (black) exhibit reduced amplitudes and faster decay relative to the CO_2-free condition (red). This systematic trend, signal suppression, and lifetime shortening in the presence of CO_2, suggest that a larger fraction of photoexcited electrons in the heterostructure undergo recombination rather than reducing adsorbed CO_2. In other words, CO_2 does not strongly bind to the $MoS_2@Cu_2O$ surface, forcing photogenerated electrons to diffuse longer distances to encounter CO_2 molecules in solution, making recombination more competitive. In addition, the accelerated decay kinetics under CO_2 indicate increased electron loss from the conduction band, consistent with electron consumption in interfacial reactions occurring away from the MoS_2 surface. This electron behavior is different from that on the Cu_2O core, where a larger population of electrons prefers to reduce CO_2 molecules rather than recombine. Also, this behavior is different from that on the MoS_2 surface, where the decay dynamics of the conduction band electrons were not affected by the presence of CO_2 molecules.

Exponential decay fitting was performed on the transient absorption dynamics to calculate the electron transfer rate. The electron transfer rate is defined as $k_{ET} = 1/t$, where t is the amplitude-weighted absorption lifetimes of the samples obtained from the fitting. Table 1 provides the electron transfer rates for each sample from Figures 5 and 6, which suggests that the electron transfer rate of $Cu_2O@MoS_2$ is slower than the electron transfer rate in the Cu_2O core but faster than that of MoS_2 flakes during the CO_2 reduction process. The accelerated charge transfer rate on $Cu_2O@MoS_2$ indicates that more CO_2 molecules were available on the catalyst surface to consume photo-excited electrons. Moreover, MoS_2 is a 2D material with excellent electron mobility, and the staggered type-II band alignment of $Cu_2O@MoS_2$ heterostructure facilitates the charge transfer from the Cu_2O core to the MoS_2 shell. The resulting abundance of electrons in the conduction band of MoS_2 can provide more electrons available to reduce CO_2. Nevertheless, the CO_2 adsorption on the surface is the kinetics limiting step. Since CO_2 molecules bind weakly on MoS_2 surfaces but strongly on Cu_2O surfaces [29], it is easier for the photogenerated electrons to transfer to CO_2 on Cu_2O surfaces than on MoS_2 surfaces due to this vicinity, hence the faster electron transfer rate on the Cu_2O surface. Consequently, the electron transfer on $Cu_2O@MoS_2$ is faster than on pure MoS_2 but slower than on Cu_2O surfaces.

These electron transfer rates and electron affinity modulation can affect the reaction pathways of CO_2 reduction. CO is the primary product for CO_2 reduction on both MoS_2 [23] and $Cu_2O@MoS_2$ heterostructures, as shown in Figure 3. However, methanol is the major product of photocatalytic CO_2 reduction on Cu_2O crystals [29]. The adsorption effect is the dominant effect on Cu_2O by the formation of chemical bonding between CO_2 and Cu_2O surfaces [29]. This strong adsorption favors multi-electron transfer processes, which lead to CO_2 reduction to CH_3OH using six electrons. Instead, the charge separation effect is the dominant effect on both MoS_2-coated Cu_2O heterostructures and MoS_2 flakes due to the weak binding of CO_2 on the MoS_2 surfaces. Therefore, CO_2 can constantly adsorb and desorb from the MoS_2 surface. Thus, the photogenerated electrons from $Cu_2O@MoS_2$ heterostructure or MoS_2 flakes need to travel a long distance to meet with CO_2 molecules to initiate the reduction reaction. This is less efficient for the multi-electron transfer process and only reduces CO_2 to CO using two electrons. Therefore, the fact that CO is the primary CO_2 reduction product on the $Cu_2O@MoS_2$ surface also proves that the heterojunction catalyst surface exhibits weak CO_2 adsorption sites, and the charge separation effect is the dominant effect. Therefore, CO_2 does not chemically absorb on $Cu_2O@MoS_2$, and we need to seek other approaches to explain the behaviors observed in the transient absorption (TA) measurements.

Density functional theory (DFT) studies were conducted to probe the electronic structures of the $Cu_2O@MoS_2$ and to investigate the absorption behaviors of CO_2. Because the Mo edge is the active site, an S vacancy is created from the MoS_2 to expose a Mo site in the structure, and the following calculations are all based on this S vacancy model. In addition, the Cu_2O core has been fully covered by the MoS_2 shell; hence, the DFT studies only probe the surface MoS_2 properties. Figure 7a,b display the charge density difference (CCD) plot in the $Cu_2O@MoS_2$ system, seen from different angles. The cyan-colored regions around Cu represent electron depletion regions, and the yellow-colored regions around Mo represent the electron accumulation region. CDD analysis confirms the electron transfer from Cu sites of Cu_2O to Mo sites of MoS_2, as predicted based on the band structures of Cu_2O and MoS_2. Figure 7c demonstrates the density of states (DOS) of pristine MoS_2 and MoS_2–Cu_2O heterostructures with DOS projected on Mo 4d and S 3p orbitals. Figure 7c suggests that because of the electron transfer from the Cu_2O core to the MoS_2 shell, the band structure of MoS_2 was altered, and the Fermi level upshifts towards a higher energy level. Similar changes in band structures of Cu_2O/MoS_2 heterojunctions have been reported in the literature [38]. Hence, it is easier to excite electrons to the conduction band, and more electrons in the conduction band can diffuse to the solution and reduce CO_2. Figure 7d illustrates the charge transfer as suggested in Figure 7c and the enhanced diffusion of electrons to the surrounding areas for CO_2 reduction reactions. Moreover, to probe the adsorption behaviors of CO_2 on MoS_2-coated Cu_2O, DFT calculations were conducted and confirmed the weak physisorption of CO_2 on both pristine MoS_2 and MoS_2-coated Cu_2O using the models shown in Figure 7e,f, respectively. DFT calculations discover slightly higher adsorption energy on MoS_2-coated Cu_2O than on bare MoS_2 (-0.15 vs. -0.13 eV), suggesting that more CO_2 can exist around the MoS_2-coated Cu_2O catalyst and consume photoexcited electrons. According to the earlier discussion, transient absorption dynamics studies indicated an increase in electron dynamics decay rates on MoS_2-coated Cu_2O when CO_2 is present in the system. Now it can be concluded that the fast decay rate is due to the high electron density in the conduction band that can supply a large population of electrons to reduce CO_2 and the slightly strengthened CO_2 physisorption that provides more CO_2 around the catalyst.

3 | Conclusion

The Cu_2O underlayer in $Cu_2O@MoS_2$ heterojunction photocatalyst plays a decisive role in the photocatalytic CO_2 reduction reaction. The electron transfer from Cu_2O to MoS_2 shell and the evolution of the electronic structure together determine the CO_2 adsorption and reaction behaviors. The carrier dynamics studies suggested that more electrons in the MoS_2 coating participated in photocatalysis due to higher local concentration of CO_2 around the catalyst surface. DFT studies further revealed that such improvements were due to the heterojunction structure between Cu_2O and MoS_2. The heterojunction not only facilitates the electron transfer from Cu_2O to MoS_2, resulting in more electrons in the conduction band of $MoS_{2,}$ but also strengthens the physisorption of CO_2 on the MoS_2 surface, thus increasing the local concentration of CO_2 molecules near the catalyst surface for CO_2 photocatalytic reduction to CO. This research employed advanced characterization techniques, such as transient absorption spectroscopy and theoretical calculations, to probe the fundamental mechanisms of heterojunction photocatalysts for CO_2 reduction. The findings provide catalyst design and characterization strategies for developing advanced heterojunction photocatalysts in the future.

4 | Experimental Section

4.1 | Synthesis of MoS_2 Coated Cu_2O byCVD

The Cu_2O core was synthesized following our previous report [29]. To synthesize Cu_2O core, deionized water (88.2 mL), $Cu(CH_3COO)_2$ aqueous solution (5 mL, 0.1 M), and sodium dodecyl sulfate (SDS, 0.87 g) were successively added into a three-

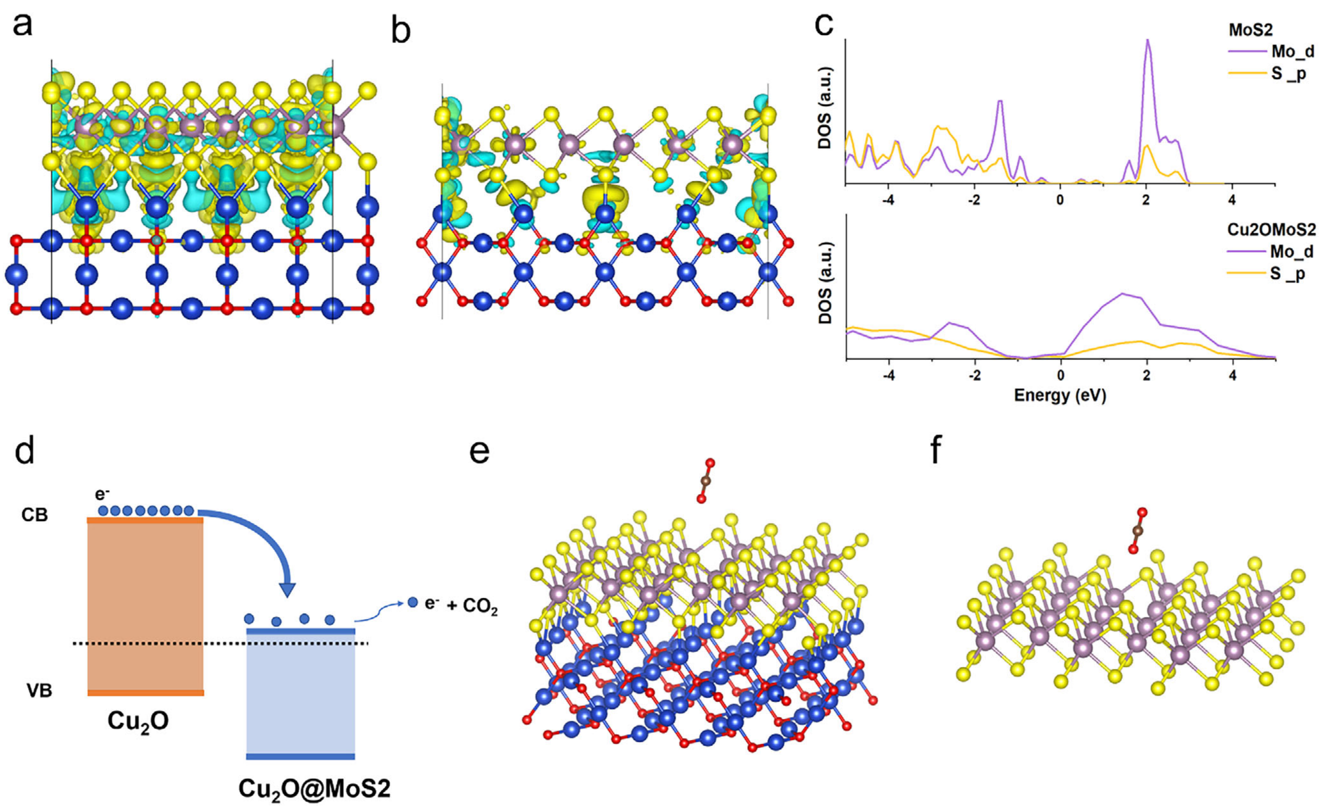

FIGURE 7 | (a) and (b) charge density difference plot in the $Cu_2O@MoS_2$ system, viewing along [010] direction and [110] direction of Cu_2O, respectively; (c) density of states (DOS) of pristine MoS_2 and $Cu_2O@MoS_2$ with DOS projected on Mo 4d orbitals and S 3p orbitals; (d) illustration of charge transfer and electron diffusion; (e) and (f) CO_2 adsorption models on MoS_2 coated Cu_2O and pristine MoS_2, respectively. The purple and yellow balls represent Mo and S atoms, respectively. The blue, red, and brown balls represent Cu, O, and C atoms, respectively.

neck flask. The three-neck flask was placed in a water bath at 60°C with vigorous magnetic stirring. After complete dissolution of the SDS powder in 1 h, NaOH solution (1.8 mL, 1.0 M) and D-(+)-glucose aqueous solution (5 mL, 0.1 M) were successively quickly injected into the flask. The total volume of solution was 100 mL. The flask was kept in a water bath at 60°C after the injection under vigorous magnetic stirring for 1 h. The solution color gradually changed from blue to green, yellow, orange, and finally brick-red. After the reaction, the precipitate was separated from the solution by centrifugation at 5000 rpm for 5 min and washed several times with deionized water/ethanol solution.

Subsequently, the particles were dispersed into one 50 mL centrifuge tube filled to 50 mL with isopropanol (IPA). Sonicate this stock solution for 30 min before dropping Cu_2O nanoparticles on a piece of clean wafer (1 × 2 cm). The clean wafer was pretreated by sonicating it in Acetone: DI (50:50) in a centrifuge tube, then repeated with IPA three times. The wafer was then placed in a vacuum oven heated to 45°C. During the drop-casting process, 5 µL of the above solution was dropped onto the wafer, followed by vacuuming the oven till the liquid on the wafer surface was fully evaporated. This process was repeated nine more times to cover all the wafer surface with Cu_2O nanoparticles, and a total of 50 µL of the above stock solution was used.

Sulfur (S, 750 mg) and molybdenum trioxide (MoO_3, 5 mg) powders were weighed and loaded into separate ends of two ceramic CVD boats. Wafer substrates (1 × 2 cm, University Wafer) dropped with Cu_2O nanoparticles were positioned face down directly above the MoO_3 precursor. A Thermo Fisher Scientific Lindberg Mini tube furnace was used for the CVD of MoS_2. The quartz boats containing S and MoO_3 were placed inside a quartz tube with an outer diameter of 25 mm and an inner diameter of 20 mm. The quartz boat containing sulfur was positioned slightly past the ceramic zone (17–18 cm from the center of the tube furnace) to control its evaporation profile. The boat containing MoO_3 was placed at the central hotspot of the furnace. After the quartz tube was sealed, it was evacuated with a vacuum pump and purged with high-purity argon (Ar) gas at a flow rate of 200 sccm, repeated three times to ensure complete air displacement. The furnace temperature was ramped from room temperature to 625 °C at a rate of 20 °C/min and held for 5 min. A further ramp to 750 °C at 30 °C/min was applied and held for 10 min. Ar flow was maintained at 200 sccm throughout the process, and the system was cooled naturally to room temperature under continued Ar flow. After cooling, the wafer was retrieved and stored under Ar atmosphere.

4.2 | Ex Situ Structural Characterization

Scanning electron microscopy (SEM) images of the photocatalyst particles were taken with a Zeiss 1540 XB FIB-SEM dual system with an acceleration voltage of 10 kV. HRTEM images were obtained with a JEOL 2100F operated at an accelerating voltage of 200 kV and equipped with a Gatan imaging filter system.

HAADF images and EDX mapping were conducted on an FEI Talos F200X scanning transmission electron microscope (STEM) with an accelerating voltage of 200 kV at the Center for Nanoscale Materials, Argonne National Laboratory. Ex situ TEM, STEM characterization was performed by drop-casting a suspension of the photocatalyst particles in ethanol onto a Formvar-coated Au TEM grid.

4.3 | Optical Spectroscopy Characterization

UV–vis absorption was measured using Perkin–Elmer Lambda 950 UV–vis spectrometer. The transient absorption spectrum was performed using a 400 nm pump and white light probe using an amplified femtosecond Ti/sapphire laser system at the Center for Nanoscale Materials, Argonne National Laboratory. A small portion of the 800 nm Ti: sapphire output was focused on a sapphire plate to produce a white light probe. The pump repetition rate was reduced to 1 kHz. Probe light was directed to a 0.3 m grating spectrograph, dispersed, and detected on a 128-element gated mercury cadmium telluride array detector. White probe full spectra were required for each laser shot, and changes in absorbance were calculated for conditions of the pump on minus pump off. Single-shot spectra were collected and averaged to produce transient absorption data. The electron transfer rate was calculated by fitting the transient absorption data to an exponential decay to extract the component that arises from CO_2 molecules by comparing the pristine and CO_2 samples.

4.4 | First-principles DFT Calculations

First-principles DFT calculations were conducted using the projected augmented wave (PAW) method [39]. The exchange-correlation functional was studied using the Perdew–Burke–Ernzerhof exchange-correlation functional of the generalized gradient approximation (PBE-GGA) [40]. All calculations applied the plane-wave expansion of the wave functions with an energy cutoff of 400 eV. During the relaxation, the force tolerance was set to 0.05 eV/Å. A Cu-terminated $Cu_2O(110)$ surface was adopted in the DFT model, where the surface Cu sites are exposed for interfacial interactions, and O atoms are in the subsurface layer. The DFT model is constructed with 4×4 units of $Cu_2O(110)$ matching 4×6 units of $MoS_2(001)$ to minimize the lattice mismatch, where a monolayer of MoS_2 sits on top of Cu_2O (110). The S atom is placed on top of the bridge between two adjacent Cu atoms with an interfacial distance of 3.5 Å. The vacuum thickness is approximately 10 Å, and the thickness of the whole slab is approximately 18.6 Å. All calculations are performed by the Vienna ab initio Simulation Package (VASP).

4.5 | Photocatalytic Activity Characterization

A piece of Si wafer coated with Cu_2O/MoS_2 heterostructure was placed in a custom-made stainless steel reaction vessel equipped with a quartz window on its top cover. The total volume of the reactor is approximately 20 mL. After the reactor was sealed and evacuated with a vacuum pump, it was repeatedly filled with Ar and evacuated three times to ensure complete air displacement. Then the reactor was filled with CO_2. 0.3 mL of ultra-pure water was then injected into the reactor through its injection port. A Xenon lamp (Perfectlight) was used to illuminate the reactor for 22 h. After the reaction, gas samples were taken via the injection port of the reactor for gas chromatography analyses, using a Shimadzu GC2020 equipped with an SH-Q-BOND column. To rule out any possible carbon contamination and background reactions, photocatalysis was conducted with a clean Si wafer, and the results were used as the baseline, which was subtracted from the results obtained with Cu_2O/MoS_2 heterostructure samples. This clean Si wafer received the same thermal treatments as the actual Cu_2O/MoS_2 samples, but without Cu_2O nanoparticles and any precursors during the pseudo CVD deposition.

4.6 | Carbon Isotope Tracer Measurements

$^{13}CO_2$ (^{13}C 99%) was purchased from Cambridge Isotope Laboratories, Inc. 0.01 g of purified particles was dispersed in 5 mL ultrapure deionized H_2O in a 20-mL Agilent Headspace vial and sealed. Then N_2 was used to purge the air from the vial for 2 min, followed by three cycles of freeze–pump–thaw to degas the photocatalyst suspension. After degassing, the $^{13}CO_2$ was introduced into the photocatalyst suspension by flushing isotope gas into the vial for 60 s. Then the samples were irradiated using a 300 W Xe lamp (Perkin–Elmer Optoelectronics, Waltham, MA) at a power of 204 W for 2 min at the same distance AS photocatalytic activity measurements. The photocatalytic product was measured using an Agilent Headspace sampler (Model 7697A) connected to an Agilent gas chromatography/mass spectrometry (GC/MS) analyzer (Model 5975C GCMS, Quadrupole detector, DB-5MS column, and helium carrier gas).

Acknowledgments

Y.A. W gratefully acknowledges the Tang Family Chair Professorship, Natural Sciences and Engineering Research Council of Canada (NSERC) (RGPIN-2020-05903, GECR-2020-00476). This research was undertaken thanks in part to funding from the Canada First Research Excellence Fund. Work performed at the Center for Nanoscale Materials, a U.S. Department of Energy Office of Science User Facility, was supported by the U.S. DOE, Office of Basic Energy Sciences, under Contract No. DE-AC02-06CH11357.

Conflicts of Interest

The authors declare no conflicts of interest.

Data Availability Statement

The data that support the findings of this study are available from the corresponding author upon reasonable request.

References

1. M. Bonchio, J. Bonin, O. Ishitani, et al., “Best Practices for Experiments and Reporting in Photocatalytic CO_2 Reduction,” *Nature Catalysis* 6 (2023): 657–665, https://doi.org/10.1038/s41929-023-00992-7.

2. S. Fang, M. Rahaman, J. Bharti, et al., “Photocatalytic CO_2 Reduction,” *Nature Reviews Methods Primers* 3 (2023): 61, https://doi.org/10.1038/s43586-023-00243-w.

3. H. He, Z. Wang, J. Zhang, C. Shao, K. Dai, and K. Fan, “Interface Chemical Bond Enhanced Ions Intercalated Carbon Nitride/CdSe-

Diethylenetriamine S-Scheme Heterojunction for Photocatalytic H_2O_2 Synthesis in Pure Water," *Advanced Functional Materials* 34 (2024): 2315426, https://doi.org/10.1002/adfm.202315426.

4. L. Liu, Z. Wang, J. Zhang, O. Ruzimuradov, K. Dai, and J. Low, "Tunable Interfacial Charge Transfer in a 2D–2D Composite for Efficient Visible-Light-Driven CO_2 Conversion," *Advanced Materials* 35 (2023): 2300643, https://doi.org/10.1002/adma.202300643.

5. S. Nishioka, F. E. Osterloh, X. Wang, T. E. Mallouk, and K. Maeda, "Photocatalytic Water Splitting," *Nature Reviews Methods Primers* 3 (2023): 42.

6. H. He, Z. Wang, J. Zhang, et al., "Enhanced Redox Kinetics for Hydrogen Peroxide Photosynthesis at High-Concentration by Encapsulating Porphyrin Metal–Organic Frameworks With Phenolic Resin," *Energy & Environmental Science* 18 (2025): 6191–6201, https://doi.org/10.1039/D5EE01295C.

7. S. Nayak and K. Parida, "Recent Progress in LDH@Graphene and Analogous Heterostructures for Highly Active and Stable Photocatalytic and Photoelectrochemical Water Splitting," *Chemistry—An Asian Journal* 16 (2021): 2211–2248, https://doi.org/10.1002/asia.202100506.

8. Y. Zheng, Z. Duan, R. Liang, et al., "Shape-Dependent Performance of Cu/Cu_2O for Photocatalytic Reduction of CO_2," *Chemsuschem* 15 (2022): e202200216.

9. S. Bai, W. Jing, G. He, et al., "Near-Infrared-Responsive Photocatalytic CO_2 Conversion via In Situ Generated Co_3O_4/Cu_2O," *ACS Nano* 17 (2023): 10976–10986, https://doi.org/10.1021/acsnano.3c03118.

10. A. Hezam, K. Alkanad, M. A. Bajiri, et al., "2D/1D MoS_2 /TiO_2 Heterostructure Photocatalyst With a Switchable CO_2 Reduction Product," *Small Methods* 7 (2023): 2201103, https://doi.org/10.1002/smtd.202201103.

11. B. Nanda, A. C. Pradhan, and K. M. Parida, "Fabrication of Mesoporous CuO/ZrO_2-MCM-41 Nanocomposites for Photocatalytic Reduction of Cr(VI)," *Chemical Engineering Journal* 316 (2017): 1122–1135, https://doi.org/10.1016/j.cej.2016.11.080.

12. S. Nayak, G. Swain, and K. Parida, "Enhanced Photocatalytic Activities of RhB Degradation and H_2 Evolution From in Situ Formation of the Electrostatic Heterostructure MoS_2 /NiFe LDH Nanocomposite Through the Z-Scheme Mechanism via p–n Heterojunctions," *ACS Applied Materials & Interfaces* 11 (2019): 20923–20942, https://doi.org/10.1021/acsami.9b06511.

13. Z. Liu, Y. Bian, G. Dawson, J. Zhu, and K. Dai, "Rational Constructing of Zn0.5Cd0.5S-diethylenetriamine/G-C_3N_4 S-Scheme Heterojunction With Enhanced Photocatalytic H_2O_2 Production," *Chinese Chemical Letters* 36 (2025): 111272, https://doi.org/10.1016/j.cclet.2025.111272.

14. C. Chen, J. Zhang, H. Chu, L. Sun, G. Dawson, and K. Dai, "Chalcogenide-Based S-Scheme Heterojunction Photocatalysts," *Chinese Journal of Catalysis* 63 (2024): 81–108, https://doi.org/10.1016/S1872-2067(24)60072-0.

15. J. Low, J. Yu, M. Jaroniec, S. Wageh, and A. A. Al-Ghamdi, "Heterojunction Photocatalysts," *Advanced Materials* 29 (2017): 1601694, https://doi.org/10.1002/adma.201601694.

16. W.-W. Dong, J. Jia, Y. Wang, et al., "Visible-Light-Driven Solvent-Free Photocatalytic CO_2 Reduction to CO by Co-MOF/Cu_2O Heterojunction With Superior Selectivity," *Chemical Engineering Journal* 438 (2022): 135622, https://doi.org/10.1016/j.cej.2022.135622.

17. L. Liu, Y. Zhang, and H. Huang, "Junction Engineering for Photocatalytic and Photoelectrocatalytic CO_2 Reduction," *Solar RRL* 5 (2021): 2000430, https://doi.org/10.1002/solr.202000430.

18. C. Cheng, J. Zhang, B. Zhu, G. Liang, L. Zhang, and J. Yu, "Verifying the Charge-Transfer Mechanism in S-Scheme Heterojunctions Using Femtosecond Transient Absorption Spectroscopy," *Angewandte Chemie International Edition* 62 (2023): e202218688, https://doi.org/10.1002/anie.202218688.

19. U. Kumar, S. D. Chakraborty, R. K. Sahu, P. Bhattacharya, and T. Mishra, "Improved Interfacial Charge Transfer on Noble Metal-Free Biomimetic CdS-Based Tertiary Heterostructure @ 2D MoS_2-CdS-Cu2O With Enhanced Photocatalytic Water Splitting," *Advanced Materials Interfaces* 9 (2022): 2101680, https://doi.org/10.1002/admi.202101680.

20. D. Nayak and R. Thangavel, "Theoretical Investigation of Electronic and Photocatalytic Properties of a Trilayer vdW MoS_2 /ZnO/WS_2 Heterojunction for Overall Water-Splitting Applications," *ACS Applied Energy Materials* 7 (2024): 2642–2652, https://doi.org/10.1021/acsaem.3c02948.

21. C. He, L. Tian, J. Hu, M. Peng, and X. Li, "Hydrogen Production From Photocatalytic Water Splitting in the hBNC/MoS_2 Heterojunction: First-Principles Calculations," *Physica B: Condensed Matter* 694 (2024): 416438, https://doi.org/10.1016/j.physb.2024.416438.

22. G. Swain, S. Sultana, J. Moma, and K. Parida, "Fabrication of Hierarchical Two-Dimensional MoS_2 Nanoflowers Decorated Upon Cubic $CaIn_2S_4$ Microflowers: Facile Approach To Construct Novel Metal-Free p–n Heterojunction Semiconductors With Superior Charge Separation Efficiency," *Inorganic Chemistry* 57 (2018): 10059–10071, https://doi.org/10.1021/acs.inorgchem.8b01221.

23. M. Asadi, B. Kumar, A. Behranginia, et al., "Robust Carbon Dioxide Reduction on Molybdenum Disulphide Edges," *Nature Communications* 5 (2014): 4470.

24. S. A. Francis, J. M. Velazquez, I. M. Ferrer, et al., "Reduction of Aqueous CO_2 to 1-Propanol at MoS_2 Electrodes," *Chemistry of Materials* 30 (2018): 4902–4908, https://doi.org/10.1021/acs.chemmater.7b04428.

25. S. Tiwari, N. Jhamb, S. Kumar, and A. K. Ganguli, "Synthesis of Photocorrosion-Resistant VS_4-MoS_2-rGO Based Nanocomposite With Efficient Photoelectrochemical Water-Splitting Activity," *ChemNanoMat* 8 (2022): e202100429.

26. C. Wu, W. Huang, H. Liu, K. Lv, and Q. Li, "Insight Into Synergistic Effect of Ti_3C_2 MXene and MoS_2 on Anti-Photocorrosion and Photocatalytic of CdS for Hydrogen Production," *Applied Catalysis B: Environmental* 330 (2023): 122653, https://doi.org/10.1016/j.apcatb.2023.122653.

27. A. Jawaid, D. Nepal, K. Park, et al., "Mechanism for Liquid Phase Exfoliation of MoS_2," *Chemistry of Materials* 28 (2016): 337–348, https://doi.org/10.1021/acs.chemmater.5b04224.

28. Y.-F. Huang, K.-W. Liao, F. R. Fahmi, et al., "Thickness-Dependent Photocatalysis of Ultra-Thin Mos2 Film for Visible-Light-Driven Co_2 Reduction," *Catalysts* 11 (2021): 1295.

29. Y. A. Wu, I. McNulty, C. Liu, et al., "Facet-Dependent Active Sites of a Single Cu_2O Particle Photocatalyst for CO_2 Reduction to Methanol," *Nature Energy* 4 (2019): 957–968, https://doi.org/10.1038/s41560-019-0490-3.

30. K. F. Mak, C. Lee, J. Hone, J. Shan, and T. F. Heinz, "Atomically Thin MoS_2: A New Direct-Gap Semiconductor," *Physical Review Letters* 105 (2010): 136805.

31. J. Kang, S. Tongay, J. Zhou, J. Li, and J. Wu, "Band Offsets and Heterostructures of Two-Dimensional Semiconductors," *Applied Physics Letters* 102 (2013): 012111, https://doi.org/10.1063/1.4774090.

32. S. S. Wilson, J. P. Bosco, Y. Tolstova, D. O. Scanlon, G. W. Watson, and H. A. Atwater, "Interface Stoichiometry Control to Improve Device Voltage and Modify Band Alignment in ZnO/Cu_2O Heterojunction Solar Cells," *Energy & Environmental Science* 7 (2014): 3606–3610, https://doi.org/10.1039/C4EE01956C.

33. C. G. Morales-Guio, S. D. Tilley, H. Vrubel, M. Grätzel, and X. Hu, "Hydrogen Evolution from a Copper (I) Oxide Photocathode Coated With an Amorphous Molybdenum Sulphide Catalyst," *Nature Communications* 5 (2014): 3059.

34. S. Xie, Q. Zhang, G. Liu, and Y. Wang, "Photocatalytic and Photoelectrocatalytic Reduction of CO_2 Using Heterogeneous Catalysts With Controlled Nanostructures," *Chemical Communications* 52 (2016): 35–59, https://doi.org/10.1039/C5CC07613G.

35. A. Brumberg, B. T. Diroll, G. Nedelcu, et al., "Material Dimensionality Effects on Electron Transfer Rates Between $CsPbBr_3$ and CdSe

Nanoparticles," *Nano Letters* 18 (2018): 4771–4776, https://doi.org/10.1021/acs.nanolett.8b01238.

36. W. N. R. W. Isahak, Z. A. C. Ramli, M. W. Ismail, et al., "Adsorption–Desorption of CO_2 on Different Type of Copper Oxides Surfaces: Physical and Chemical Attractions Studies," *Journal of CO2 Utilization* 2 (2013): 8–15, https://doi.org/10.1016/j.jcou.2013.06.002.

37. N. Yu, L. Wang, M. Li, X. Sun, T. Hou, and Y. Li, "Molybdenum Disulfide as a Highly Efficient Adsorbent for Non-Polar Gases," *Physical Chemistry Chemical Physics* 17 (2015): 11700–11704, https://doi.org/10.1039/C5CP00161G.

38. Y.-F. Zhao, Z.-Y. Yang, Y.-X. Zhang, et al., "Cu_2O Decorated With Cocatalyst MoS_2 for Solar Hydrogen Production With Enhanced Efficiency Under Visible Light," *Journal of Physical Chemistry C* 118 (2014): 14238–14245, https://doi.org/10.1021/jp504005x.

39. J. Taylor, M. Brandbyge, and K. Stokbro, "Theory of Rectification in Tour Wires: The Role of Electrode Coupling," *Physical Review Letters* 89 (2002): 138301.

40. J. P. Perdew, K. Burke, and M. Ernzerhof, "Generalized Gradient Approximation Made Simple," *Physical Review Letters* 77 (1996): 3865–3868, https://doi.org/10.1103/PhysRevLett.77.3865.